

DNA dynamics as inferred from Tethered Particle Motion: experiments *vs* simulations

Manoel Manghi,^{†‡1} Catherine Tardin,^{§¶1} Julien Baglio,^{†‡§¶} Philippe
Rousseau,^{||**} Laurence Salomé,^{§¶} and Nicolas Destainville^{†‡*}

[†] *Université de Toulouse; UPS; Laboratoire de Physique Théorique (IRSAMC); F-31062
Toulouse France;* [‡] *CNRS; LPT (IRSAMC); F-31062 Toulouse France;* [§] *CNRS;
IPBS (Institut de Pharmacologie et Biologie Structurale) 205 route de Narbonne,
F-31077 Toulouse France;* [¶] *Université de Toulouse; UPS; IPBS; F-31077 Toulouse
France;* ^{||} *Université de Toulouse; UPS; Laboratoire de Microbiologie et Génétique
Moléculaires; F-31062 Toulouse France;* and ^{**} *CNRS; LMGM; F-31062 Toulouse France.*

¹ *M. Manghi and C. Tardin contributed equally to this work.*

(Dated: July 18, 2022)

The Tethered Particle Motion (TPM) technique informs about conformations of DNA molecules by tracking the Brownian motion of a particle probe tethered to a surface by a single DNA molecule. By comparing theory, simulations and experiments, we propose a calibration of TPM at the dynamical level. We focus on the particle-DNA complex relaxation time, i.e. the characteristic time it takes to explore its configuration space by diffusion. We analyze how this time grows with both DNA contour length (from 400 to 2000 base pairs) and particle radius (from 20 to 150 nm). We also demonstrate that for a particle of radius less than 20 nm, this time is identical for a DNA observed by TPM and a DNA fluctuating freely in solution: the hydrodynamic friction induced by the particle or the surface do not significantly slow down the DNA. We also explain how the exposure time and the acquisition period of the detector used to track the particle must be chosen to get exploitable data. Finally, we discuss the time resolution of TPM when used to probe DNA conformation changes such as looping or bending upon protein binding.

INTRODUCTION

Biophysical techniques at the single molecule level have become an integral part of the available toolbox to investigate biomolecular machineries. The rapid development of experimental techniques for the exploration of conformations and dynamics of single DNA molecules emphasizes the need for suitable theoretical tools to interpret the large amount of data collected. Among the many techniques used in biology or biophysics laboratories, Tethered Particle Motion (TPM) [1–12] is very promising because it explores the *equilibrium* statistical mechanics of the biopolymer in the absence of external force, by contrast to optical or magnetic tweezers experiments [13]. One end of a DNA molecule is immobilized on a glass surface, and the other end is attached to a particle, the diameter of which ranges from a few tens to several hundreds of nanometers (Fig. 1). Tracking by video-microscopy the particle trajectory informs about DNA conformations, in particular its end-to-end distance (or “effective length”), in real time. Hence TPM also gives access to *dynamical* properties at the time-scale of one second. Getting insights into the dynamics of biomolecular events is of great significance. Should its time resolution be sufficient, TPM has the capability to access the dynamics of DNA conformational changes, such as looping [3–5, 12], bending due to protein binding [3, 12, 15], hybridization [16], or changes induced by enzyme processing [1, 2]. We discuss below that the precise experi-

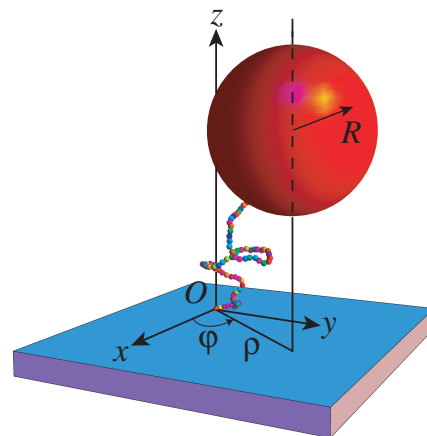


FIG. 1: Snapshot of TPM Monte-Carlo simulation: The tethered DNA molecule is modeled as a coarse-grained chain of N connected spheres (various hues), fixed to the glass surface at one end and to the tracked particle at the other end. Here, $N = 80$, the DNA contour length is $L = 2080$ base pairs ($\simeq 700$ nm) and the particle radius is $R = 150$ nm. Only the polar coordinates ρ and φ in the (xy) plane are accessible by conventional TPM.

mental conditions, especially the proximity of the surface and the attachment of the particle, are likely to perturb the polymer, both at the statistical and dynamical levels. The purpose of the present work is to quantify these effects and to foresee when they are negligible.

Effects on DNA conformations in equilibrium have already been the focus of several analytical, numerical, and experimental works [7–10, 14]. We revisit how the projected particle excursion scales with particle radius and

*Correspondence: nicolas.destainville@irsamc.ups-tlse.fr

DNA length, by using smaller particles, with radii down to 20 nm, for DNA molecules of length L ranging between a few hundreds and a few thousands of base-pairs (bp; 1 bp = 0.34 nm). The DNA is semi-flexible since L is on the order of the persistence length, $\ell_p \simeq 150$ bp.

To our knowledge, dynamical consequences of the setup geometry, in particular of the attached particle, have not been quantified extensively yet. Calibration of TPM experiments on DNA remains to be performed at the dynamical level. To this end, we combine TPM experiments and dynamical Monte Carlo simulations that take into account hydrodynamic effects in the vicinity of the surface. Comparing both data sets, we demonstrate that the surface and the particle do not affect significantly the polymer dynamics provided that the particle radius R remains small as compared to the DNA contour length. More quantitatively, for the polymers considered in this work, this condition amounts to $R \lesssim 20$ nm. In addition we address rigorously a critical instrumental issue: the detectors used in TPM experiments always have a finite exposure time, ranging from milli-seconds to a fraction of second [8, 9, 17–19]. We show that experimental studies must take into account the finiteness of this exposure time in order to extract valuable data. We finally discuss the intrinsic time resolution of TPM experiments when monitoring DNA conformational changes.

MATERIALS AND METHODS

Tethered Particle Motion (TPM) Experiments

DNA substrates were obtained by PCR amplification from plasmid templates with a 21-digoxigenin-modified forward primer and a 21-biotin-labelled reversed primer (Eurogentec) as described in Ref. [6]. The DNA substrates DNAR401, DNAR798, DNAR1500, DNARL2080 were produced using pAPT72 as a template (positions: 1460-1861, 1063-1861, 361-1861, 4625-1861, respectively). Their lengths are $L = 401, 798, 1500$ and 2080 bp respectively.

Experiments with fluorescent latex particles of radii 20 and 100 nm (Fluospheres Neutravidin, Molecular Probes) were performed using a protocol similar to the one described in Ref. [6]. A coverslip flow chamber (30 μ L volume) was incubated with the anti-digoxigenin antibody (20 mg/L; Roche) in phosphate-buffered saline (PBS) for 20 min at room temperature. After washing, the chamber was incubated with casein (1 g/L) in PBS at 4°C for 4 hours. Experiments with the $R = 150$ nm particles (Anti-dig fluorescent particles, Indicia) were performed using chambers whose surfaces were derivatized with a mixture of polyethylene glycol and biotinylated polyethylene glycol (Sigma, Nanocs) based on the protocol of Ref. [20]. The chamber was incubated with neutravidin (20 mg/L, Molecular Probes) in PBS for 20 min at room temperature. The chamber was subsequently rinsed and incubated with the mix of DNA and neutravidin (20 nm, 100 nm) or anti-dig (150 nm) coated particles (ratio 1:1, 1 pM) that had been prepared 1 hour before in PBS with 0.1 g/L BSA. Due to the lack of small particles coated with antiDig, we could not use the PEG passivated coverslips, known to reduce unspecific binding of DNA-particle complex on the glass, in all the conditions.

The tethered particles of 150 nm (resp. 100 nm and 20 nm) were visualized by fluorescence video-microscopy, with a magnification of 63x4x, on a CCD camera Coolsnap (resp. Cascade, RoperScientific) at a recording time of 25 frames/s (resp. 74 frames/s and 112

frame/s), which corresponds to an acquisition period T_{ac} equal to 40 ms (resp. 13.5 ms and 8.9 ms). In all cases, we could restrict the exposure time T_{ex} to 5 ms by the use of an AOTF (or by entering such a command in the acquisition parameters of the Cascade CCD).

Particle position was determined on successive images as the spot centroid using a home built image analysis program (Labview). The trajectories exhibiting asymmetry were discarded following [21]. Furthermore, a minority of trajectories appeared to have an amplitude of movement $\Delta \mathbf{r}^2$ significantly shorter than the remaining ones, which yields a bimodal distribution of $\Delta \mathbf{r}^2$ with a small population of low amplitudes. These trajectories, that might also be related to multi-DNA-particle complexes, have been discarded. The final number of trajectories for each condition (L, R, T_{ex}, T_{ac}) ranges from 19 to 60. Details are given in the Supporting Material. Trajectories have an average duration of 90 s. Along a trajectory, the DNA anchoring point at time t is determined by averaging the particle position over an interval of duration $T_{av} = 2$ s centered at t . This subtracts the instrumental drift. Since T_{av} is much larger than the diffusion relaxation time (see below), this anchoring point is determined with a good accuracy. The accuracy of the position detection (pointing error), calculated as the standard deviation of the positions of immobilized particles accumulated during 30 s, is equal to 36, 21, and 8 nm for the particles of radius 20, 100, and 150 nm respectively.

DNA coarse-grained model

The labeled DNA polymer is modeled as a chain of N connected small spheres of radius a , whose positions are denoted by $\mathbf{r}_i(t)$ where $i = 0, \dots, N-1$, and a larger final particle of radius $R \geq a$, of position $\mathbf{r}(t)$ (see Figs. 1 and SM.1). The DNA contour length is $L = 2a(N-1)$. In this work, a ranges between 1.4 and 7 nm, and R between 0 (i.e. no particle) and 150 nm. The internal structure of the double-stranded DNA is not considered at this level of modeling. Denaturation bubbles are too scarce at room temperature to have an effect on the global chain conformation [22, 23]. The persistence length value $\ell_p = 147$ bp is averaged over the nucleotide sequence. Torsional degrees of freedom are omitted as a first hint into the full problem. The polymer is grafted on a surface which sets $\mathbf{r}_0 = 0$. Due to the geometry of the experiment, it is convenient to use cylindrical coordinates (ρ, φ, z) : $\mathbf{r} = \rho \mathbf{e}_\rho + z \mathbf{e}_z = \mathbf{r}_\parallel + z \mathbf{e}_z$. Since the polymer motion is limited to the upper half-plane, we impose the following “hard wall” boundary conditions: $z_i > 0$ for monomer spheres and $z > R - a$ for the particle. Furthermore, we choose to treat theoretically and numerically a freely rotative joint to the glass coverslip [7], by fixing the first sphere center at a height a above the surface. However, it might happen that, for special types of experimental constructions, the joint is better modeled as a rigid anchor (clamped polymer). In this case, the first two spheres are fixed perpendicularly to the surface.

All spheres interact *via* stretching and bending forces: the potential U is the discrete version of the *extensible* worm-like chain potential and depends on the sphere positions \mathbf{r}_i and the particle one \mathbf{r} as $U = \sum_{i=0}^{N-2} \left[\frac{\gamma}{4a} (|\mathbf{r}_i - \mathbf{r}_{i+1}| - 2a)^2 + \frac{\varepsilon}{2a} (1 - \cos \theta_i) \right] + \frac{\gamma}{4a} (|\mathbf{r}_{N-1} - \mathbf{r}| - R)^2 + \frac{\varepsilon}{2a} (1 - \cos \theta_{N-1})$ where θ_i is the angle between neighbouring bonds of sphere i . The first term ensures the polymer connectivity and the second term is the bending energy with zero spontaneous curvature. The last two terms are dedicated to the particle. The parameters γ and ε are the stretching and bending moduli [24]. The persistence length is given by $\ell_p = \varepsilon/(k_B T)$. We choose $\gamma a^2 = 4\varepsilon$, which is exact for an isotropic elastic cylinder with radius a . Therefore the key parameters in the simulation are L/ℓ_p , R and N . Mutual penetration of monomers is prevented by an excluded volume interaction.

A fully realistic description would be to fix the sphere radius, a , equal to the DNA half-width, i.e. about 1 nm. Hence one sphere would model roughly 6 bp and 25 spheres would correspond to the

typical DNA persistence length of 150 bp at physiological temperature and salt concentration. Time limitation in the simulations led us to concentrate on $N = 50$ (or 25) for a DNA of 400 to 2000 bp and thus to choose $a > 1$ nm. As far as equilibrium properties are concerned, the DNA statistical mechanics are insensitive to the choice of N , provided that a remains small as compared to ℓ_p , so that a sphere represents a DNA segment that is actually rigid.

Dynamical Monte Carlo simulations

Out-of-equilibrium dynamics can be tackled numerically by Dynamical Monte Carlo (DMC) simulations that become equivalent to Brownian dynamics when the variation of energy at each time step, ΔU , satisfies $\Delta U \ll k_B T$ [25]. We have also performed Brownian dynamics simulations of the system which yield very similar results on statistical and dynamical properties (see Supporting Material). At each Monte Carlo Step (MCStep) of physical duration δt , a bead is chosen uniformly at random among the $N + 1$ possible ones (monomer spheres and labeling particle). Then a random move $\delta \mathbf{r}$ is attempted for this bead, uniformly in a ball of center 0 and radius R_b , thus $\langle \delta \mathbf{r}^2 \rangle = 4\pi \int_0^{R_b} r^4 dr / 4\pi \int_0^{R_b} r^2 dr = (3/5)R_b^2$. This quantity must be equal to $6D_0\delta t$, where D_0 is the diffusion coefficient of the spherical bead, depending on its diameter (see previous section). In practice, for monomer spheres, $R_b = a/5$, where a is their radius. Then δt is chosen subsequently, and R_b for the particle is fixed in turn because it is slower than monomer spheres. Interactions between adjacent beads are treated *via* the interaction potential energy U , whereas interactions between non-adjacent beads are of hard core nature, like surface-bead interactions: whenever a move would lead to the penetration of a bead into an other one or the surface, it is rejected. A Monte Carlo Sweep (MCS) is a sequence of $N + 1$ MCSteps. The physical time is incremented of δt following each MCS [25]. Typically, a simulation lasts between 10^9 and 10^{10} MCS, which leads to satisfactory error bars, estimated by usual techniques [25] (see also Eq. 10). In the simulations, $N = 50$ or 25, depending on the slowness of the physical process. Since $a \ll \ell_p$ in all cases, we expect that dynamics do not depend on N either. A simulation snapshot is shown in Fig. 1.

Diffusion near the surface: hydrodynamic effects

The motion of a spherical particle is slowed down near a flat surface due to the no-slip condition for the solvent velocity flow at the wall. The induced hydrodynamic interactions cause a variation, with the distance to the surface, of the diffusion coefficient as compared to its bulk value D_0 . This new diffusion tensor can be split into a component parallel to the wall, D_{\parallel} , and a perpendicular component, D_{\perp} . For a sphere of radius b (here $b = a$ or R), the center of which is at a distance h from the wall, parallel and perpendicular diffusion coefficients are derived from Faxén's law [26]. At order 3 in b/h ,

$$\begin{aligned} D_{\perp} &= D_0 \left(1 - \frac{9}{8} \frac{b}{h} + \frac{1}{2} \frac{b^3}{h^3} \right) \\ D_{\parallel} &= D_0 \left(1 - \frac{9}{16} \frac{b}{h} + \frac{1}{8} \frac{b^3}{h^3} \right). \end{aligned} \quad (1)$$

Monte Carlo simulations must be modified to take into account these spatially varying diffusion coefficients. First of all, random moves $\delta \mathbf{r}$ are now randomly chosen in an ellipsoid to account for anisotropy. In addition, careful attention must be paid to the discretization of the equations of motion in this case. A vertical drift term $(dD_{\perp}/dh)\mathbf{e}_z$ must be added to compensate the variation of D_{\perp} with h and to restore the detailed balance condition [27]. As a consequence, this improvement of dynamics does not affect equilibrium properties such as chain statistics.

Extracting relaxation times from experimental and numerical data

A key observable in polymer dynamics is the relaxation or correlation time. It corresponds to the time taken by the chain to explore its whole configuration space by diffusion, and can also be seen as the time after which the memory of the initial condition is lost. We focus here on the relaxation time τ_{\parallel} associated with the two-dimensional projection \mathbf{r}_{\parallel} of the particle center-of-mass because it is the only quantity accessible to conventional TPM experiments. It is computed through the two-time correlation function averaged over a trajectory:

$$C(t) = \langle \mathbf{r}_{\parallel}(s+t) \mathbf{r}_{\parallel}(s) \rangle_s \approx \langle \mathbf{r}_{\parallel}^2 \rangle \exp(-t/\tau_{\parallel}), \quad (2)$$

if one assumes without loss of generality that $\langle \mathbf{r}_{\parallel} \rangle = 0$. Alternatively, the 2D Mean Square Deviation (MSD) is:

$$\begin{aligned} \text{MSD}(t) &= \langle (\mathbf{r}_{\parallel}(s+t) - \mathbf{r}_{\parallel}(s))^2 \rangle_s = 2\langle \mathbf{r}_{\parallel}^2 \rangle - 2C(t) \\ &\approx 2\langle \mathbf{r}_{\parallel}^2 \rangle [1 - \exp(-t/\tau_{\parallel})]. \end{aligned} \quad (3)$$

At short times $t \ll \tau_{\parallel}$, one expects to recover the 2D diffusion law $\text{MSD}(t) = 4Dt$, with D the apparent particle 2D diffusion coefficient. Thus the correlation time for this particle in a 2D trap with variance $\Delta \mathbf{r}_{\parallel}^2 = \langle \mathbf{r}_{\parallel}^2 \rangle$ is taken to be [17]

$$\tau_{\parallel} = \frac{\Delta \mathbf{r}_{\parallel}^2}{2D}. \quad (4)$$

Relaxation times are fitted from simulated trajectories after computing $C(t)$ and $\text{MSD}(t)$, using Eqs. 2-3, leading to two relaxation times, τ_C and τ_{MSD} . The values used below are the mean values $\tau_m = (\tau_C + \tau_{\text{MSD}})/2$, and the error bars are the half-distances $|\tau_C - \tau_{\text{MSD}}|/2$. In practice, fits are performed on an interval $t \in [0, t_{\text{sup}}]$. Since numerical error bars on $C(t)$ and $\text{MSD}(t)$ are larger and larger as t grows, the smallest possible value of t_{sup} must be used. On the other hand, for $\text{MSD}(t)$, one must have t_{sup} larger than a few τ_{MSD} in order to fit properly the exponential decay. We have chosen $t_{\text{sup}} = 4\tau_{\text{MSD}}$, which is a good compromise between both constraints. The fitting procedure, consisting in fitting τ_{MSD} on $[0, t_{\text{sup}}]$ and then adjusting $t_{\text{sup}} = 4\tau_{\text{MSD}}$, is iterated a few times until τ_{MSD} is converged. Similarly, τ_C is obtained by measuring the slope of $\ln[C(t)/C(0)] \simeq -t/\tau_C$, on the interval $[0, \tau_C]$, with the same iterative procedure. However, in some instances ($R \leq 20$ nm), $\ln[C(t)/C(0)]$ appears to display a short transient, equal to a small fraction of τ_C , because of slow diffusion modes. In this case, linear regressions are performed on a suitably chosen interval $[t_{\text{inf}}, \tau_C]$, where they appear to be very good.

For experimental data, τ_{\parallel} is fitted from $C(t)$ as follows. The raw correlation function averaged over all available trajectories is denoted by $C_{\text{raw}}(t)$. The systematic pointing error is taken into account: the detected position, $\mathbf{r}_{\parallel, \text{raw}}$, is the sum of the actual position, \mathbf{r}_{\parallel} and the pointing error, \mathbf{r}_e , two independent random variables. Thus $\Delta \mathbf{r}_{\parallel, \text{raw}}^2 = \langle \mathbf{r}_{\parallel, \text{raw}}^2 \rangle = \langle \mathbf{r}_{\parallel}^2 \rangle + \langle \mathbf{r}_e^2 \rangle$. The second contribution is systematically subtracted from measured values $\Delta \mathbf{r}_{\parallel, \text{raw}}^2 \equiv C_{\text{raw}}(0)$, using the pointing error values as given above. This modified correlation function is denoted by $C_m(t)$. In addition, the subtraction of drift induces systematic anti-correlations at short times leading to the following fitting form

$$\frac{C_m(t)}{C_m(0)} = \left(1 + 2 \frac{\tau_m}{T_{\text{av}}} \right) e^{-t/\tau_m} - 2 \frac{\tau_m}{T_{\text{av}}}, \quad (5)$$

with a *single* fitting parameter, τ_m . The fits are systematically very good for all the data sets considered. The prescription is the same as above: the fitting interval $[0, t_{\text{sup}}]$ is chosen so that $t_{\text{sup}} = 4\tau_m$. Error bars on τ_m correspond to the standard deviation of the measurements on individual trajectories.

Correction of detector time-averaging effects

Finally, one has to correct time-averaging effects in experimental results. In Refs. [8, 9, 17–19], the time-averaging (or blurring) effect due to the finite exposure time of detectors in single molecule (or particle) tracking experiments was investigated. It can have important consequences on the experimental apparent motion of tracked molecules or particles when they diffuse in confined regions. This effect was quantified by exact analytical arguments in Ref. [17]: diffusion constants can be significantly under-estimated, as well as sizes of confining domains. In the present work, the situation is similar because the motion of the particle is restricted by the DNA tether. The difference is that here the confining potential is essentially quadratic, whereas it was uniform in a bounded region of space in the previous studies. However, all the analytical derivation of Ref. [17] remains valid in the 2D quadratic case and the real relaxation time $\tau_{||}$, domain size (or root-mean-square excursion from the attachment point) $\Delta \mathbf{r}_{||}$ and diffusion coefficient D can be related to their measured counterparts, τ_m , $\Delta \mathbf{r}_{||,m} \equiv \sqrt{C_m(0)}$ and D_m . Whenever $\tau_m \geq 2 T_{\text{ex}}/3$

$$\tau_{||} \simeq \tau_m - T_{\text{ex}}/3, \quad (6)$$

where T_{ex} is the detector exposure time, and

$$\Delta \mathbf{r}_{||} = \Delta \mathbf{r}_{||,m} \left[2 \frac{\tau_{||}}{T_{\text{ex}}} - 2 \left(\frac{\tau_{||}}{T_{\text{ex}}} \right)^2 \left(1 - e^{-\frac{T_{\text{ex}}}{\tau_{||}}} \right) \right]^{-1/2}. \quad (7)$$

If $\tau_m < 2 T_{\text{ex}}/3$, this formalism cannot be applied and one ought to switch to a faster acquisition device.

RESULTS AND DISCUSSION

Equilibrium distributions of particle positions

We first analyze the particle positions at equilibrium by plotting the histograms of projected particle excursions, $\rho = |\mathbf{r}_{||}|$, i.e. the probability distribution $p(\rho)$. We focus on DNA lengths $L = 401, 798, 1500$ and 2080 bp, corresponding to the semi-flexible case ($2 < L/\ell_p < 14$) which cannot be handled analytically. The theoretical study of the limiting cases, rigid rod ($L \ll \ell_p$) and flexible chain ($L \gg \ell_p$), is reported in the Supporting Material. In addition to the experimental particle radii $R = 20, 100$ and 150 nm, we also examined numerically the radius $R = 80$ nm, as well as $R = 0$ (no particle).

Simulation results – The criterion $a \ll \ell_p$ is satisfied for all DNA lengths if $N = 50$. However for small DNA molecules ($L \leq 798$ bp), some calculations were performed choosing $N = 25$ to save computational time, and in this case we have checked that the distributions coincide within statistical noise. In particular, the fact that monomer spheres are in general larger than the actual radius of the DNA molecule ($a > 1$ nm) does not affect significantly our physical observables. This observation is related to the questions of polymer self-avoidance and solvent quality: in our simulations, the short range repulsion, which is essentially of electrostatic origin, is taken into account by the sphere hard-core repulsion, the effective range of which is thus larger than the bare DNA diameter. Moreover, there exist attractive interactions, mediated by the solvent, between two DNA segments

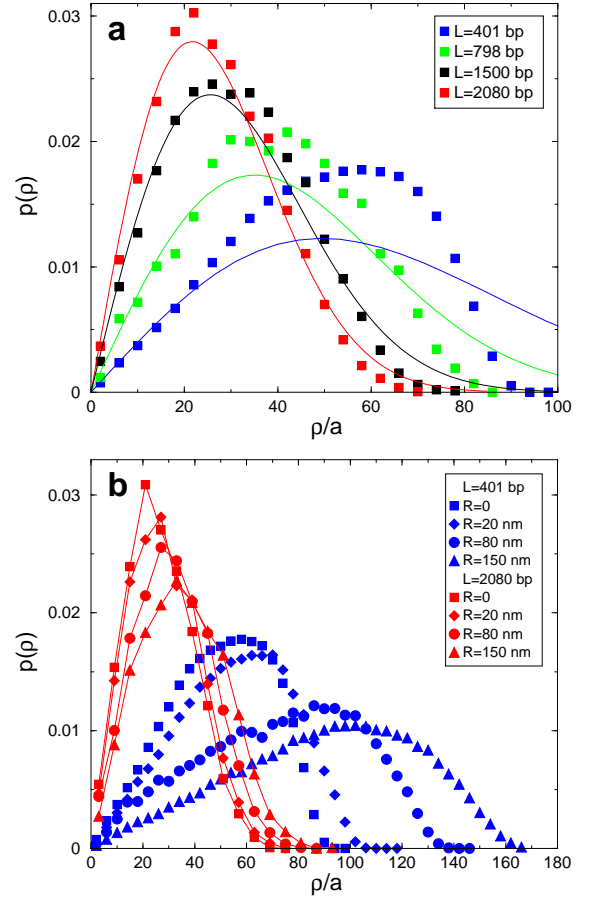


FIG. 2: Numerical chain statistics $p(\rho)$, ρ in units of a ($N = 50$). (a) Symbols represent the normalized histograms for $R = 0$ and $L = 401, 798, 1500$ and 2080 bp and continuous lines the Gaussian distributions for the same values of L . (b) Normalized histograms for $L = 401$ and 2080 bp and different values of R . Lines are guides for eyes.

which are far away along the chain. They are of hydrophobic nature [28, 29] since water is a bad solvent for DNA. We assume monovalent counter-ions and do not consider situations where DNA condensation occurs [30]. These interactions are relevant for long DNAs which are flexible at large length scales and can be neglected in this work, because the average number of sphere contacts is extremely small as L/ℓ_p remains moderate. Therefore the choice of a appears to be an irrelevant issue as far as chain statistics are concerned, provided that $a \ll \ell_p$.

Fig. 2 displays numerical distributions $p(\rho)$. Fig. 2a shows $p(\rho)$ when the particle radius $R = 0$. When L is large the numerical distributions and the Gaussian ones (details in Supporting Material) are superimposed. This observation supports our previous remarks about the rareness of DNA self-contacts, as self-avoidance is not taken into account in the Gaussian approximation. When L decreases, numerical distributions deviate from Gaussians: they are skewed to the right with a steep decrease near ρ_{max} , a signature of the rigid-rod distribution (see

Fig. S2a). Fig. 2b shows the same histograms for $L = 401$ and 2080 bp where R varies between 0 and 150 nm. For $L = 2080$ bp, the distributions look like Gaussian for all the values of R studied, but are slightly shifted to larger ρ and widened, as compared to the phantom chain case (see Supporting Material), due to self-avoidance between the particle and the chain. For $L = 401$ bp, the steep decrease of the distributions near ρ_{\max} get smoothed when R increases.

Finally, in order to quantify the effect of the surface, we have also simulated DNAs with no surface, rotating freely in the whole space around their attachment point (at $\mathbf{r}_0 = 0$). For the four DNA lengths considered in this work, no effect on the distribution of ρ has been detected (by contrast, z is obviously perturbed by the wall). Note that in both the rigid and Gaussian regimes, this result is shown analytically in Eqs. S6,S10,S11. It appears to be also valid in the intermediate semi-flexible regime.

Correction of detector time-averaging effects in experimental results – In experiments, the detector has a finite exposure time T_{ex} . The ensuing time-averaging effect is known to affect both dynamical and statistical measurements if T_{ex} is on the order of (or greater than) the DNA-particle relaxation time τ_{\parallel} : the diffusion of the particle appears slower in a smaller domain [17], and the distributions $p(\rho)$ look like Gaussian even if they are not, especially in the semi-flexible regime. The mathematical correction of this effect, when possible, is presented in the Methods Section (see Eqs. 6 and 7). These formulae enable us to compare the instantaneous values coming from numerical simulations, which do not suffer from any averaging effects, with those extracted from experiments. Note that in Ref. [6], time-averaging effects were not suitably corrected and the amplitude of movements were slightly underestimated.

This correction scheme is rigorous contrary to the rough approximation of Eq. 7 proposed by Ref. [9]. The formula given in this anterior work largely overestimates the averaging effect, thus requiring the introduction of a phenomenological parameter (their time scale τ^*).

Comparison between experimental and numerical distributions – Fig. 3 compares two distributions $p(\rho)$ extracted from both TPM experiments and simulations (additional graphs in Figs. S3 and S4). The agreement is systematically good, even though some discrepancies appear. In order to quantify further these small discrepancies, we plot in Fig. 4 the values of the standard deviations $\Delta\mathbf{r}_{\parallel} = \langle \mathbf{r}_{\parallel}^2 \rangle^{1/2}$ as a function of L . Interpolating functions evaluated from Monte Carlo simulations have been proposed that give $\Delta\mathbf{r}_{\parallel}$ in function of L , R and ℓ_p [8]. We have checked that our numerical results are in agreement with these interpolations when $R = 100$ or 150 nm, even though they were calibrated for $R > 190$ nm. For $R = 20$ nm, these interpolating functions are less reliable.

In Fig. 4, one observes that except for the smallest $R = 20$ nm particles, experimental $\Delta\mathbf{r}_{\parallel}$ are shorter than sim-

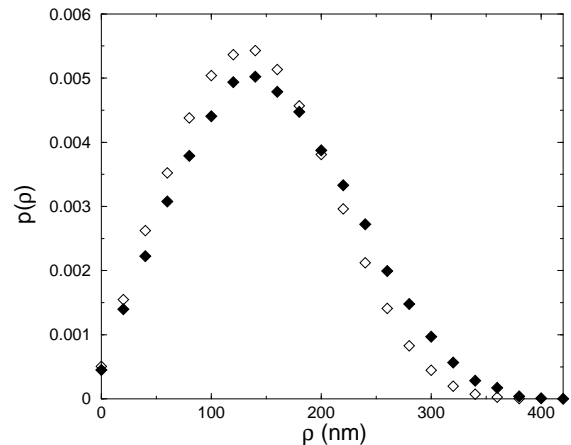


FIG. 3: Experimental (open symbols) and numerical (solid symbols) chain statistics $p(\rho)$ for $R = 20$ nm and $L = 1500$ bp.

ulated ones. Nelson *et al.* [8] have already noticed that assuming the persistence length $\ell_p = 50$ nm in data analysis leads to larger $\Delta\mathbf{r}_{\parallel}$ than observed. To circumvent this issue, they pointed out that setting $\ell_p = 43.4$ nm yields better agreement, attributing this low value to the buffer. We also observe that setting $\ell_p = 43.4$ nm leads to values of $\Delta\mathbf{r}_{\parallel}$ closer to our experimental observations for $R = 150$ nm. However for $R = 20$ nm, the correction goes into the wrong direction. Note that the actual value of ℓ_p is certainly not the unique source of discrepancy between theory and experiments. For example, the interaction between the functionalized surface on the one hand, and the particle (and DNA) on the other hand, is more complex than a simple excluded volume one. The fact that at $R = 20$ nm, $\ell_p = 43.4$ nm is no longer an adequate value corroborates this point of view. Therefore inferring a precise value of ℓ_p from such experiments is a challenging task [10]. Given the approximations used in the physical modeling, we simply conclude that the agreement with experiments is satisfactory because the discrepancies are lesser than 15%.

Relaxation times of the DNA-particle complex

In this section, we compare the relaxation times τ_{\parallel} extracted from both experimental and numerical trajectories (see Methods). In our Dynamical Monte Carlo (DMC) simulations, moves are local (one bead at once). This choice is more time-consuming than the global Monte Carlo sampling of Refs. [8, 14], but has the advantage to give access to dynamical properties, which is the main goal of the present work.

We first present general considerations on dynamical properties of a DNA fluctuating freely in solution. We then give basic insights into the influence of the attached particle. We finally address the full issue on the particle-DNA-surface system, both experimentally and numeri-

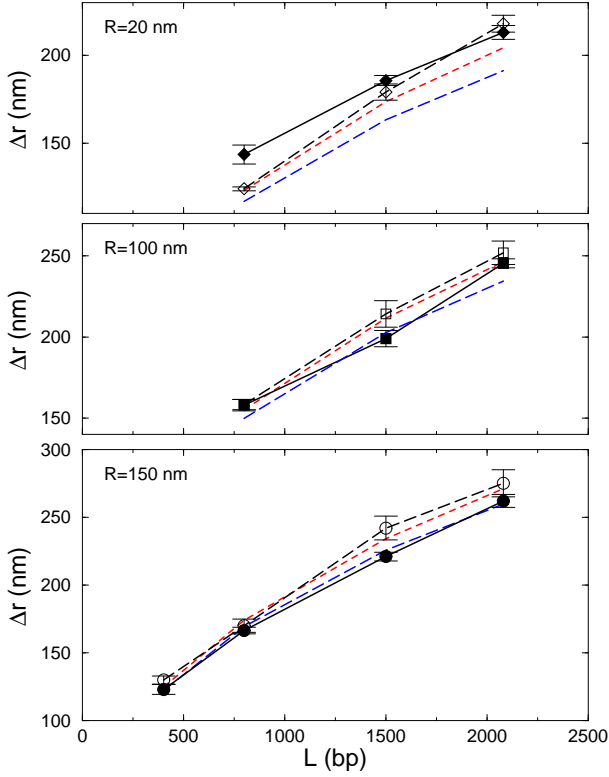


FIG. 4: Comparison between experimental (solid symbols) and numerical (open symbols) standard deviations $\Delta \mathbf{r}_{\parallel} = \langle \mathbf{r}_{\parallel}^2 \rangle^{1/2}$. Experimental values have been corrected from systematic errors. Error bars are 95 % confidence intervals. Red and blue dashed lines are predictions from Ref. [8] for $\ell_p = 50$ and 43.4 nm, respectively.

cally.

Relaxation times and diffusion coefficients – For a polymeric chain, without attached particle, of radius of gyration R_G , the correlation time is evaluated to $\tau_{\parallel} \simeq R_G^2/D_{\text{chain}} = NR_G^2/D_0$ [31]. In the second equality, we have used the Rouse model ignoring hydrodynamic interactions and valid for very flexible chains ($L/\ell_p \gg 1$), which sets $D_{\text{chain}} = D_0/N$ where $D_0 = k_B T/(6\pi\eta a)$ is the diffusion coefficient of a monomer sphere, given by Stokes' formula in a liquid of viscosity η . For a Gaussian chain, $R_G^2 \propto N$ and we get $\tau_{\parallel} \sim N^2/D_0$ at large N . For a rigid rod, $R_G^2 \propto N^2$ and $\tau_{\parallel} \sim N^3/D_0$.

To which respect does the replacement of the real polymer by connected monomer spheres in simulations affect the correlation time? R_G being insensitive to the choice of a as discussed previously, the only dependence in N comes from the ratio N/D_0 in τ_{\parallel} . But with the definition of D_0 , $N/D_0 \propto Na \propto L$, independently of a . The last relation ensues from $Na = L/2$, valid when $a \ll \ell_p$. Therefore at the level of modeling chosen in the present work, dynamics should not be affected by the choice of N if $a \ll \ell_p$.

How is this chain relaxation time modified when the

particle is grafted? To answer this question, we relate the diffusion coefficient of the particle-DNA complex, D_c , to those of the particle alone, D_{part} , and the DNA polymer alone, D_{chain} . The time evolution of these two objects is governed by the over-damped Langevin equation [24, 31]

$$\zeta_i \dot{\mathbf{r}}_i(t) = -\nabla_{\mathbf{r}_i} U(\mathbf{r}_0, \dots, \mathbf{r}_{N-1}, \mathbf{r}_{\text{part}}) + \boldsymbol{\xi}_i(t), \quad (8)$$

where i stands for spheres ($i = 0, \dots, N-1$) or the particle ($i = N$) (we neglect hydrodynamic interactions as a first hint into the full problem). This equation relates the linear response of each object i to forces applied to it: on the one hand, the derivative of the potential U (sum of pairwise potentials) between the N objects; on the other hand, the stochastic forces $\boldsymbol{\xi}_i(t)$ mimic the action of a thermal heat bath and obeys the fluctuation-dissipation relation: $\langle \boldsymbol{\xi}_i(t) \cdot \boldsymbol{\xi}_j(t') \rangle = 6k_B T \zeta_i \delta(t-t') \delta_{ij}$, where the friction coefficient ζ_i ($= \zeta_0$ for monomer spheres and $\zeta_0 R/a$ for the particle) is related to the diffusion coefficient D_i through $D_i = k_B T/\zeta_i$.

The only way to get rid of the interaction forces in a linear combination of Langevin equations 8 is to consider the barycenter $\mathbf{r}_c = (\zeta_{\text{chain}} \mathbf{r}_{\text{chain}} + \zeta_{\text{part}} \mathbf{r}_{\text{part}})/\zeta_c$ where $\mathbf{r}_{\text{chain}} = \sum \mathbf{r}_i/N$ is the DNA center of mass. Then $\zeta_c \dot{\mathbf{r}}_c(t) = \boldsymbol{\xi}_c(t)$, where $\boldsymbol{\xi}_c = \boldsymbol{\xi}_{\text{chain}} + \boldsymbol{\xi}_{\text{part}}$. The correlation function $\langle \boldsymbol{\xi}_c(t) \cdot \boldsymbol{\xi}_c(t') \rangle = 6k_B T \zeta_c \delta(t-t')$ sets D_c :

$$D_c^{-1} = D_{\text{part}}^{-1} + D_{\text{chain}}^{-1}. \quad (9)$$

In general, D_c should not be confused with the measured effective particle coefficient, D , because $\mathbf{r}_c \neq \mathbf{r}_{\text{part}}$. However, in the limiting case $D_{\text{part}} \ll D_{\text{chain}}$ (and thus $\zeta_{\text{part}} \gg \zeta_{\text{chain}}$), \mathbf{r}_c and \mathbf{r}_{part} coincide and $D_c = D_{\text{part}} = D$. By contrast, τ_{\parallel} , as defined above, is a feature of the dynamics of the whole complex, even though it is obtained by tracking the particle only. Therefore we will focus on this observable in the following.

Simulation results without hydrodynamic interactions – We first display in Fig. 5 the relaxation times fitted from numerical trajectories simulated without hydrodynamic interactions with the surface. They are denoted by $\tau_{\parallel,0}^{\text{sim}}$. We checked that finite- N effects appear to be negligible for $a \ll \ell_p$. We also explored the reference case $R = 0$, where no particle is attached to DNA. We have seen above that the Rouse model predicts $\tau_{\parallel} \sim L^2$ at large L . Fig. 5 shows that this regime is also a good approximation even for the finite sizes considered here. We also plot in Fig. 5 the relaxation times in the previously mentioned case where $R = 0$ in the absence of hard wall at $z = 0$. One can see that, within error bars, the wall does not hinder DNA dynamics.

When $R > 0$, the particle slows down dynamics because viscous drag increases with the particle size. However our simulations predict that DNAs are not significantly affected for a small particle ($R = 20$ nm) or for an intermediate particle ($R = 80$ nm) and long DNAs ($L \geq 1500$ bp). In the other cases, increasing R from 0 to 150 nm at fixed L monotonically increases $\tau_{\parallel,0}^{\text{sim}}$, by a factor ranging from 2 ($L = 2080$ bp) to 10 ($L = 401$ bp).

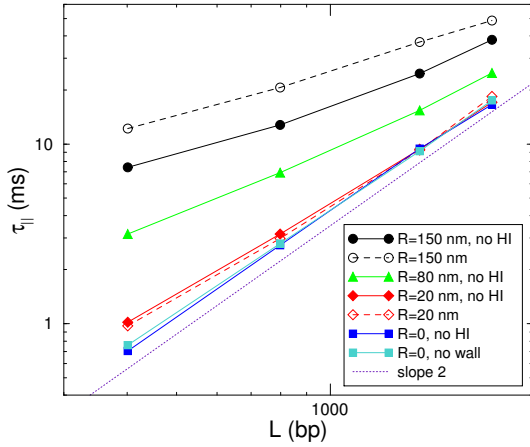


FIG. 5: Numerical relaxation time $\tau_{||,0}^{\text{sim}}$ (solid lines: without wall hydrodynamic friction (no HI); $N = 50$, except for $L = 401$ bp and $R = 150$ nm where $N = 25$) and $\tau_{||}^{\text{sim}}$ (dashed lines: with wall hydrodynamic friction; $N = 25$ for $L = 401$ and 798 bp, $N = 50$ for $L = 1500$ and 2080 bp) versus the polymer length L for various particle sizes R , in log-log coordinates. In the case $R = 0$, $\tau_{||}$ is also plotted when there is no hard wall. The dotted line of slope 2 shows the expected scaling for long DNAs (Rouse model for a random walk).

Simulation results with hydrodynamic interactions with the surface – Hydrodynamic interactions between the particle-DNA complex and the surface are implemented in the numerical code using Eq. 1. Fig. 5 shows that the diffusion is slowed down by hydrodynamic corrections for large particles ($R = 150$ nm) but is not affected for smaller ones ($R = 20$ nm). Indeed, small particles are far away from the surface, in that sense that $R \ll z$ and $b/h = R/(z + a)$ is generically small in Eq. 1. Only the first DNA spheres, for which $b/h = a/(z_i + a)$ is of order 1, are slowed down by the proximity of the surface but this is not sufficient to affect the whole dynamics. This is related to the observation that the exact modeling of the DNA-surface joint is not a relevant issue (see Supporting Material). By contrast, when R is large, $R/(z + a)$ is close to 1 for the particle itself, and hydrodynamic corrections play a significant role.

Comparison between experimental and numerical relaxation times – Fig. 6 displays our experimental (accounting for detector averaging effects using Eq. 6) and numerical values of the relaxation times $\tau_{||}$ extracted from functions $C(t)$ or $\text{MSD}(t)$ (Methods). Experimental and numerical values are in good agreement, with ratios of experimental to numerical values varying from 0.5 to 2. These ratios are plotted in the Inset of Fig. 6 and appear to be well correlated to the ratios L/R and to follow the approximate power-law: $\tau_{||}^{\text{exp}}/\tau_{||}^{\text{sim}} \propto (R/L)^{1/3}$. This indicates that the observed discrepancies are not due to statistical errors (as supported by the smallness of error-bars), but certainly have a more fundamental origin. When $R \ll L$, $\tau_{||}^{\text{exp}} < \tau_{||}^{\text{sim}}$, i.e. experiments are

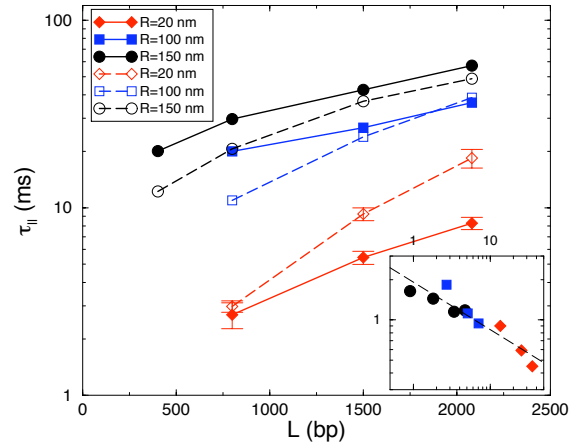


FIG. 6: Experimental ($\tau_{||}^{\text{exp}}$, solid symbols) and numerical ($\tau_{||}^{\text{sim}}$, using z -dependent diffusion coefficients, open symbols) relaxation times for different DNA lengths, L , and particle radius, R , in linear-log coordinates. Displayed error bars are explained in the text for numerical data and are 95 % confidence intervals for experimental data. Other error bars are smaller than symbol sizes. *Inset*: Ratio $\tau_{||}^{\text{exp}}/\tau_{||}^{\text{sim}}$ versus L/R with the same symbols as above, in log-log coordinates. The dashed line shows the best linear regression, with slope $-0.355 \simeq -1/3$.

faster than simulations. If $R \geq L/5$, then $\tau_{||}^{\text{exp}} \geq \tau_{||}^{\text{sim}}$. Indeed, if one neglects hydrodynamics, the measured diffusion coefficient of the particle-DNA complex, D_c , is related to the particle one, D_{part} , and to the polymer one, D_{chain} , through Eq. 9: $D_c^{-1} = D_{\text{part}}^{-1} + D_{\text{chain}}^{-1}$. Thus the particle does not slow down the complex provided that $D_{\text{part}} \gg D_{\text{chain}}$. Now $D_{\text{part}} = K/R$ with $K = k_B T / (6\pi\eta)$, and $D_{\text{chain}} = K/(Na) = 2K/L$ in the Rouse approximation. If $2R \ll L$, then $D_{\text{part}} \gg D_{\text{chain}}$ and the DNA dominates the particle-DNA dynamics, as if the particle were absent. But in this case, hydrodynamic interactions between DNA segments should be taken into account. Since such interactions are known to accelerate polymer dynamics [24, 31], one expects $\tau_{||}$ to be shorter than in our simulations, as indeed observed in experiments. Conversely, if $2R \gg L$, then the particle dominates the particle-DNA dynamics, as if the role of the DNA polymer was limited to its spring properties. We have simplified the complex hydrodynamics of this particle in the vicinity of a wall through the expansions in Eq. 1. But these expansions are valid in the small b/h limit only and we cannot expect them to be correct when $b/h \simeq 1$, which is the case when $2R \gg L$. In Ref. [26] Section 7-4, it is demonstrated that Eq. 1 overestimates D_{\perp} and $D_{||}$ in this case. Consequently, $\tau_{||}$ is underestimated as observed. Describing correctly the particle dynamics in this case would require a full integration of all hydrodynamic interactions, between the monomer spheres, the particle and the surface, which is out of the scope of the present work.

L(bp)	T_{ex} (ms)	τ_{m} (ms)	$\Delta \mathbf{r}_{\parallel, \text{m}}$ (nm)	τ_{\parallel} (ms)	$\Delta \mathbf{r}_{\parallel}$ (nm)
2080	40	69.5	223	56.1	250
	5	59.1	258	57.4	261
401	40	32.8	91	19.5	122
	5	21.7	118	20.0	123

TABLE I: Relaxation times and movement amplitudes before (τ_{m} and $\Delta \mathbf{r}_{\parallel, \text{m}}$) and after correction (τ_{\parallel} and $\Delta \mathbf{r}_{\parallel}$) of detector time averaging effects, using Eqs. 6-7, for two DNA lengths L and two exposure times T_{ex} . Here the particle radius is $R = 150$ nm.

Choice of TPM parameters to infer DNA dynamics

The preceeding analysis leads us to suggest the following recommendations to extract the most valuable information on DNA dynamics from TPM experiments.

Small particles of radius $R \lesssim 20$ nm do not slow down DNAs as small as 400 bp – Comparing $R = 0$ and $R > 0$ data, we have observed in our simulations (Fig. 5) that for small particles or long DNAs, the presence of the particle or the wall does not increase relaxation times. Indeed, we have shown that dynamics are dominated by the polymer provided that $R \ll L/2$, in agreement with our observations: Fig. 5 shows that if $R < L/6$ then τ_{\parallel} is less than twice the relaxation time of DNA without particle, which demonstrates that slowing-down is weak or moderate in this case. In particular, slowing down is very weak when $R = 20$ nm for $L = 401$ to 2080 bp.

Hydrodynamics has three contributions: i) slowing down of the chain and the particle, due to the no-slip condition at the surface, ii) hydrodynamic interactions between the chain and the particle, and iii) interactions between monomer spheres. For creeping flows, these three effects contribute linearly [26]. We have shown above that, for small R , (i) affects only very weakly the relaxation times. Contributions (ii) and (iii), which are not taken into account in simulations, moderately accelerate the dynamics of the particle-DNA complex, as shown by experimental values (diamonds in Fig. 6). By linearity, we thus expect that neither the wall nor the small particle slows down DNA dynamics as compared to DNA fluctuating freely in solution.

Taking into account exposure times and acquisition periods – In the Methods section, we have explained how the finiteness of the exposure time, T_{ex} , modifies the relaxation time, τ_{\parallel} , root-mean-square excursion of the particle, $\Delta \mathbf{r}_{\parallel}$, and particle diffusion coefficient, D , and we have prescribed how to recover their real values. To this respect, we have observed two particle-DNA complexes ($R = 150$ nm and $L = 2080$ and 401 bp) with two different exposure times, $T_{\text{ex}} = 5$ and 40 ms and the same acquisition period $T_{\text{ac}} = 40$ ms in both cases. The measured values before applying Eqs. 6,7 and after correction are given in Table I. For the two exposure times, we observe that the values after correction are in excellent agreement for both DNA lengths. These values validate

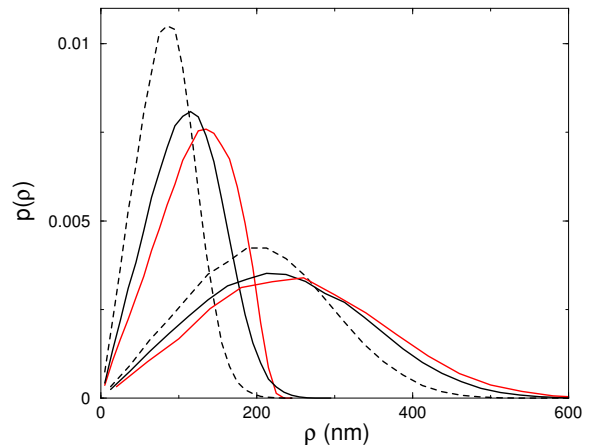


FIG. 7: Comparison of experimental chain statistics $p(\rho)$ for two exposure times, $T_{\text{ex}} = 5$ (solid black lines) and 40 ms (dashed lines). For comparison, solid red lines correspond to numerical distributions. Left curves: $R = 150$ nm and $L = 401$ bp; and right curves: $R = 150$ nm and $L = 2080$ bp. Histograms are represented by lines for clarity.

our method to correct detector averaging effects on experimental data.

Beyond their width $\Delta \mathbf{r}_{\parallel}$, probability distributions $p(\rho)$ are also affected when T_{ex} becomes larger than τ_{\parallel} , as shown in Fig. 7. In particular, because of the central-limit theorem, their Gaussian character is restored when $T_{\text{ex}} \gg \tau_{\parallel}$, even though the real distributions are far from Gaussian in the rigid or semi-flexible regime. But recovering real distributions from their measured counterparts is a difficult task that is out of scope of the present work: it requires to de-convolute the averaging effect, which depends not only on ρ but also on z , because diffusion time-scales are \mathbf{r} -dependent. The examination of Eqs. 6,7 reveals that in order to reduce averaging effects, it suffices to lower the exposure time T_{ex} . When $T_{\text{ex}} \ll \tau_{\parallel}$, averaging effects become negligible. But we have shown in this paper that the *a priori* determination of the adapted values of T_{ex} is not an easy task because the calculation of τ_{\parallel} cannot rely on simple assumptions [10]. Our values of τ_{\parallel} given in Fig. 6 will help experimentalists to anticipate the appropriate required values of the exposure time T_{ex} in future works. However, reducing T_{ex} becomes insufficient when one is interested in measuring τ_{\parallel} . The acquisition period T_{ac} being imposed by the camera, the only points available to fit $\text{MSD}(t) \propto [1 - \exp(-t/\tau_{\parallel})]$ or $C(t) \propto \exp(-t/\tau_{\parallel})$ plots are measured at discrete values $t = 0, T_{\text{ac}}, 2T_{\text{ac}}$ and so forth. But if T_{ac} remains too large as compared to τ_{\parallel} , $\text{MSD}(T_{\text{ac}})$ and $C(T_{\text{ac}})$ have already reached their asymptotic values, respectively $2\Delta \mathbf{r}_{\parallel}^2$ and 0, making any fitting procedure hopeless. If one is interested in dynamical properties, the true technical limit obviously remains the camera acquisition period, which must satisfy $T_{\text{ac}} \lesssim 2\tau_{\text{m}}$.

Measuring variations of $\langle \mathbf{r}_{\parallel}^2 \rangle$ in real time – Beyond the

measurement of equilibrium statistics or relaxation rates, TPM experiments can also be used to monitor DNA conformational changes. To what extent can those conformational changes be monitored in real time? In TPM, such a change is characterized by a variation of the movement amplitude, $\Delta \mathbf{r}_{\parallel}^2 = \langle \mathbf{r}_{\parallel}^2 \rangle$, due to a given molecular event such as protein binding or DNA looping, leading to a shortening of the apparent DNA length. But measuring the mean value $\langle \mathbf{r}_{\parallel}^2 \rangle$ supposes to average \mathbf{r}_{\parallel}^2 on a sufficiently long time interval, of duration again denoted by T_{av} [3]. By definition of the relaxation time τ_{\parallel} , the average will be accurate provided that $T_{\text{av}} \gg \tau_{\parallel}$. Once τ_{\parallel} is known, what averaging time T_{av} should be chosen in practice? In other words, what is the minimum time scale of conformational changes that TPM can address? Formally speaking, $\langle \mathbf{r}_{\parallel}^2 \rangle \simeq \int_{t_0}^{t_0+T_{\text{av}}} \mathbf{r}_{\parallel}^2(t) dt / T_{\text{av}}$. The decorrelation time of \mathbf{r}_{\parallel}^2 , $\tau_{\parallel,2}$, is again defined by $\langle \mathbf{r}_{\parallel}^2(s+t)\mathbf{r}_{\parallel}^2(s) \rangle_s - \langle \mathbf{r}_{\parallel}^2 \rangle^2 \approx \sigma_{\mathbf{r}_{\parallel}^2}^2 \exp(-t/\tau_{\parallel,2})$ (we use the notation $\sigma_{\mathbf{r}_{\parallel}^2}$ for the r.m.s. of \mathbf{r}_{\parallel}^2 , to avoid confusion with $\Delta \mathbf{r}_{\parallel}^2$, the variance of \mathbf{r}_{\parallel}). Then the statistical error on the measurement of $\langle \mathbf{r}_{\parallel}^2 \rangle$, denoted by $\text{Err}(\mathbf{r}_{\parallel}^2)$, can be quantified as follows [25]: if $\tau_{\parallel,2} \gtrsim T_{\text{ac}}$, then $\text{Err}(\mathbf{r}_{\parallel}^2) = \sqrt{2\tau_{\parallel,2}/T_{\text{av}}} \sigma_{\mathbf{r}_{\parallel}^2}$. This relation takes into account statistical correlations between successive frames, measured by $\tau_{\parallel,2}$. If $\tau_{\parallel,2} \ll T_{\text{ac}}$, then $\text{Err}(\mathbf{r}_{\parallel}^2) = \sqrt{T_{\text{ac}}/T_{\text{av}}} \sigma_{\mathbf{r}_{\parallel}^2}$, because all frames are statistically independent.

Now, what is the relationship between $\tau_{\parallel,2}$ and τ_{\parallel} ? Since $\mathbf{r}_{\parallel}^2 = x^2 + y^2$, $\tau_{\parallel,2} = \tau_{x^2} = \tau_{y^2}$, the (identical) decorrelation times of the observables x^2 and y^2 . If x and y were Gaussian random variables, then $\tau_{x^2} = \tau_x/2 = \tau_{\parallel}/2$. But x is not exactly Gaussian. In practice, we have measured numerically in our case that $\tau_{\parallel,2} \simeq \tau_{\parallel}/c$ with c ranging from 2.5 to 3.5, depending on L and R . Thus $\tau_{\parallel,2} \leq \tau_{\parallel}/2$. Furthermore, we have also measured numerically that $\sigma_{\mathbf{r}_{\parallel}^2} < \langle \mathbf{r}_{\parallel}^2 \rangle$ for the values of L and R studied here. Were \mathbf{r}_{\parallel} be exactly Gaussian, a simple calculation shows that $\sigma_{\mathbf{r}_{\parallel}^2} = \langle \mathbf{r}_{\parallel}^2 \rangle$ (because \mathbf{r}_{\parallel} is two-dimensional). Thus in the regime where $\tau_{\parallel,2} \gtrsim T_{\text{ac}}$,

$$\frac{\text{Err}(\mathbf{r}_{\parallel}^2)}{\langle \mathbf{r}_{\parallel}^2 \rangle} < \sqrt{\frac{\tau_{\parallel}}{T_{\text{av}}}}. \quad (10)$$

For example, if $T_{\text{ac}} = 10$ ms and $\tau_{\parallel} \approx 20$ ms, a relative error $\text{Err}(\mathbf{r}_{\parallel}^2)/\langle \mathbf{r}_{\parallel}^2 \rangle$ of 10% is achieved provided that $T_{\text{av}} \geq 100 \tau_{\parallel} \approx 2$ s. If the explored conformational changes lead to variations of \mathbf{r}_{\parallel}^2 much larger than 10%, they can be detected in real time provided that their time scale is higher than 2 s. Using shorter DNAs, smaller particles, and a faster acquisition device improves this limit. If $R = 20$ nm and $L = 401$ bp, $T_{\text{av}} = 300$ ms suffices to obtain the same relative error of 10%, which falls down to 5% if $T_{\text{av}} = 1$ s. A concrete illustrative example is given in Fig. S5.

CONCLUSION

This work focuses on the influence on DNA statistics and dynamics of the TPM setup geometry, namely the attachment of the DNA tether to, on one end the surface and, on the other end the labeling particle. To what extent DNA characteristic times and diffusion constant can be inferred from TPM observations? This complex issue cannot be summarized in simple formulas because many parameters are involved and interrelated, in particular: the particle size R , the DNA contour length L , the DNA persistence length ℓ_p , the exposure time T_{ex} , the acquisition period T_{ac} , and the averaging time T_{av} . To answer this question, we used numerical simulations whose results were compared with a set of experimental data. A good quantitative agreement (see Figs. 4 and 6) leads us to two major conclusions, summarizing the last section of our Results and Discussion, where experimental constraints on dynamical TPM are surveyed.

1) For DNA lengths L usually used in TPM experiments, i.e., from hundreds to thousands base pairs, the DNA dynamics is weakly perturbed by particles of radius $R = 20$ nm or less. Indeed, in this case, hydrodynamic friction induced by the particle and the surface are weak and the DNA characteristic relaxation time in the plane parallel to the surface, τ_{\parallel} , is almost identical to the case where the particle and the surface are absent. Note that for this parameter range ($2R \ll L$), the slower object is the DNA tether, and the diffusion constant of the particle-DNA complex is essentially equal to the DNA one. Accordingly, TPM experiments focusing on DNA dynamics, where large particles ($R \gg 20$ nm) are used, must be re-examined by accounting for the dynamics of the labeling particle.

2) In the TPM analysis of DNA conformational changes, the use of particles of radius smaller than 20 nm allows to detect events with characteristics times as short as 300 ms within a statistical error of 10%. We believe that such a substantial improvement of the time resolution will provide a more detailed view on DNA-protein interaction processes involving DNA bending [3, 12, 15], looping [3–5, 12] or migration of a Holliday junction [2] in the future.

On the theoretical side, the scaling law of the ratio of the experimental relaxation times to numerical ones in $(R/L)^{1/3}$ (see Fig. 6) provides a clue that hydrodynamic interactions play a crucial role. Brownian dynamics simulations (see Supporting Material) will be the next step in order to elucidate this issue. They ought to include: 1) hydrodynamic interactions between beads [24, 32], usually taken into account through the Rotne-Prager tensor; and 2) hydrodynamic images induced by the presence of the particle and the surface to ensure the no-slip condition on these surfaces [24].

We thank Denis Gotta for his participation to this work as part of his Science Degree project, Vincent Croquette and Rob Philipps for stimulating discussions.

-
- [1] Schafer, D. A., J. Gelles, M. P. Sheetz, and R. Landick. 1991. Transcription by single molecules of RNA polymerase observed by light microscopy. *Nature*. 352:444–448.
- [2] Dennis, C., A. Fedorov, E. Kas, L. Salomé, and M. Grigoriev. 2004. RuvAB-directed branch migration of individual Holliday junctions is impeded by sequence heterology. *EMBO J.* 23:2413–2422.
- [3] Pouget, N., C. Turlan, N. Destainville, L. Salomé, and M. Chandler. 2006. IS911 transpososome assembly as analysed by tethered particle motion. *Nucl. Acids Res.* 34:4313–4323.
- [4] Zurla, C., T. Samuely, G. Bertonni, F. Valle, G. Dieter, L. Finzi, and D. D. Dunlap. 2007. Integration host factor alters LacI-induced DNA looping. *Biophys. Chem.* 128:245–252.
- [5] Rutkauskas, D., H. Zhan, K. S. Matthews, F. S. Pavone, and F. Vanzi. 2009. Tetramer opening in LacI-mediated DNA looping. *Proc. Natl. Acad. Sc. USA*. 106:16627–16632.
- [6] Pouget, N., C. Dennis, C. Turlan, M. Grigoriev, M. Chandler, and L. Salomé. 2004. Single-particle tracking for DNA tether length monitoring. *Nucleic Acids Res.* 32:e73.
- [7] Seol, Y., J. Li, P. C. Nelson, T. T. Perkins, and M. D. Betterton. 2007. Elasticity of short DNA molecules: theory and experiment for contour lengths of 0.67 μm . *Biophys. J.* 93: 4360–4373.
- [8] Nelson, P. C., C. Zurla, D. Brogioli, J. F. Beausang, L. Finzi, and D. D. Dunlap. 2006. Tethered Particle Motion as a diagnostic of DNA tether length. *J. Phys. Chem. B*. 110:17260–17267.
- [9] Towles, K. B., J. F. Beausang, H. G. Garcia, R. Phillips, and P. C. Nelson. 2009. First-principles calculation of DNA looping in tethered particle experiments. *Phys. Biol.* 6:025001.
- [10] Brinkers, S., H. R. C. Dietrich, F. H. de Groote, I. T. Young, and B. Rieger. 2009. The persistence length of double stranded DNA determined using dark field tethered particle motion. *J. Chem. Phys* 130:215105.
- [11] Han, L., H. G. Garcia, S. Blumberg, K. B. Towles, J. F. Beausang, P. C. Nelson, and R. Phillips. 2009. Concentration and length dependence of DNA looping in transcriptional regulation. *PLoS ONE* 4:e5621.
- [12] Laurens, N., S. R. W. Bellamy, A. F. Harms, Y. S. Kovacheva, S. E. Halford, and G. J. L. Wuite. 2009. Dissecting protein-induced DNA looping dynamics in real time. *Nucleic Acids Res.* 37:5454–5464.
- [13] Bustamante, C., Z. Bryant, and S. B. Smith. 2003. Ten years of tension: single-molecule DNA mechanics. *Nature* 421:423–427.
- [14] Segall, D. E., P. C. Nelson, and R. Phillips. 2006. Volume-excluded effects in tethered-particle experiments: bead size matters. *Phys. Rev. Lett.* 96:088306.
- [15] Dixit, S., M. Singh-Zocchi, J. Hanne, and G. Zocchi. 2005. Mechanics of binding of a single integration-host-factor protein to DNA. *Phys. Rev. Lett.* 94:118101.
- [16] Singh-Zocchi, M., S. Dixit, V. Ivanov, and G. Zocchi. 2003. Single-molecule detection of DNA hybridization. *Proc. Natl. Acad. Sc. USA* 100:7605–7610.
- [17] Destainville, N. and L. Salomé. 2006. Quantification and correction of systematic errors due to detector time-averaging in single-molecule tracking experiments. *Biophys. J.* 90:L17–L19.
- [18] Allemand, J.-F. 1997. Micromanipulation d’une molécule individuelle d’ADN. Ph.D. Thesis. Université Pierre et Marie Curie, Paris.
- [19] Savin, T., and P. S. Doyle. 2005. Static and dynamic errors in particle tracking micro-rheology. *Biophys. J.* 88:623–638.
- [20] Cuvelier, D., O. Rossier, P. Bassereau, and P. Nassoy. 2003. Micropatterned “adherent/repellent” glass surfaces for studying the spreading kinetics of individual red blood cells onto protein-decorated surfaces. *Eur. Biophys. J.* 32:342–354.
- [21] Blumberg, S., A. Gajraj, M. W. Pennington, and J.-C. Meiners. 2005. Three-Dimensional Characterization of Tethered Microspheres by Total Internal Reflection Fluorescence Microscopy. *Biophys. J.* 89:1272–1281.
- [22] Palmeri, J., M. Manghi, and N. Destainville. 2007. Thermal denaturation of fluctuating DNA driven by bending entropy. *Phys. Rev. Lett* 99:088103.
- [23] Destainville, N., M. Manghi, and J. Palmeri. 2009. Microscopic mechanism for experimentally observed anomalous elasticity of DNA in two dimensions, *Biophys. J.* 96:4464–4469.
- [24] Manghi, M., X. Schlagberger, Y.-W. Kim, and R. R. Netz. 2006. Hydrodynamic effects in driven soft matter, *Soft Matter* 2:653–668.
- [25] Newman, M. E. J., and G. T. Barkema. 1999. Monte Carlo Methods in Statistical Mechanics. Clarendon Press, Oxford.
- [26] Happel, J., and H. Brenner. 1983. Low Reynolds Number Hydrodynamics. Martinus Nijhoff Publishers, The Hague.
- [27] Ermak, D. L., and McCammon J. A. 1978. Brownian dynamics with hydrodynamic interactions. *J. Chem. Phys.* 69:1352–1360.
- [28] Strey, H. H., R. Podgornik, D. C. Rau, and V. A. Parsegian. 1998. DNA-DNA interactions. *Cur. Opinion Struct. Biol.* 8:309–313.
- [29] Odijk, T. 1994. Long range attraction in polyelectrolyte solutions. *Macromol.* 27:4998–5003.
- [30] Bloomfield, V. A. 1996. DNA condensation. *Cur. Opinion Struct. Biol.* 6:334–341.
- [31] Doi, M., S. F. Edwards. 1986. The theory of Polymer Dynamics. Oxford University Press, Oxford.
- [32] Petrov, E. P., T. Ohrt, R. G. Winkler, and P. Schwiile. 2006. Diffusion and segmental dynamics of double-stranded DNA. *Phys. Rev. Lett.* 97:258101.

Supporting material to the paper DNA dynamics as inferred from Tethered Particle Motion: experiments *vs* simulations

Manoel Manghi, Catherine Tardin, Julien Baglio,
Philippe Rousseau, Laurence Salomé, and Nicolas
Destainville

Tethered Particle Motion (TPM) Experiments

The number of experimental particle trajectories followed in TPM experiments for various DNA lengths L , exposure times T_{ex} and particle radii R (in nm) are given in the following table:

DNA length L (bp)	$T_{\text{ex}} = 40$ ms $R = 150$	$T_{\text{ex}} = 5$ ms		
		$R = 20$	$R = 100$	$R = 150$
401	46			32
798		34	24	32
1500		38	19	40
2080	33	60	41	29

Fitting procedure

The fitting procedure to extract the relaxation time τ_{\parallel} from experimental data is presented in the Section Material and Methods of the paper. An alternative way to circumvent systematic errors on $C_{\text{raw}}(0)$ consists of excluding $C_{\text{raw}}(0)$ in the fitting procedure and using the fitting formula

$$C_{\text{raw}}(t) = \Delta \mathbf{r}_{\text{m},\parallel}^2 \left[\left(1 + 2 \frac{\tau_{\text{m}}}{T_{\text{av}}} \right) e^{-t/\tau_{\text{m}}} - 2 \frac{\tau_{\text{m}}}{T_{\text{av}}} \right], \quad (\text{S1})$$

with two free parameters, $\Delta \mathbf{r}_{\text{m},\parallel}^2$ and τ_{m} . For all data sets, the so-obtained values of τ_{m} are equal, within a few percents, to the ones coming from Eq. (5), thus confirming the validity of our fitting procedure.

Brownian Dynamics simulations

For the numerical iterations, the evolution of each sphere position $\mathbf{r}_i(t)$ is governed by an iterative Langevin equation with a discrete time step δt . In terms of the discrete time variable $n = t/\delta t$,

$$\tilde{\mathbf{r}}_i(n+1) = \tilde{\mathbf{r}}_i(n) - \tilde{D}_0 \nabla_{\tilde{\mathbf{r}}_i} \tilde{U}(n) + \sqrt{2\tilde{D}_0} \tilde{\xi}_i(n), \quad (\text{S2})$$

where the rescaled random displacement has variance unity $\langle \tilde{\xi}_i(n) \cdot \tilde{\xi}_j(m) \rangle = 3 \delta_{ij} \delta_{nm}$. The rescaled bare diffusion coefficient $\tilde{D}_0 = D_0 \delta t / a^2$ is the diffusion constant in an unbounded space in units of the particle radius a

and time step δt : a sphere typically takes $1/\tilde{D}_0$ iterations to diffuse on a distance a . For sufficient numerical accuracy we choose time steps in the range $\tilde{D}_0 = 10^{-3} - 10^{-5}$ to avoid unphysical large displacements and forces. Output values are calculated every $10^3 - 10^4$ steps, total simulation times are on the order of $10^8 - 10^9$ steps, giving reasonable error bars. Finally, since the polymer motion is limited to the upper half-plane $z > 0$, we use the following reflection boundary condition: if a sphere intersects the substrate, its height z_i is replaced by z_i^{refl} :

$$z_i < a \Rightarrow z_i^{\text{refl}} = 2a - z_i \quad \text{for } i < N \quad (\text{S3})$$

$$z_N < R - a \Rightarrow z_N^{\text{refl}} = 2(R - a) - z_N \quad (\text{S4})$$

The excluded volume interaction is modeled by a repulsive, truncated Lennard-Jones potential $\tilde{U}_{LJ} = \sum_{i < j} [(b/|\tilde{\mathbf{r}}_i - \tilde{\mathbf{r}}_j|)^{12} - 2(b/|\tilde{\mathbf{r}}_i - \tilde{\mathbf{r}}_j|)^6 + 1]$ valid for separation $|\tilde{\mathbf{r}}_i - \tilde{\mathbf{r}}_j| < 2$ and $b = \tilde{R} + 1$ for $j = N$ and $b = 2$ otherwise.

Comparison between Brownian Dynamics and dynamical Monte Carlo simulations

We have simulated our particle-DNA complex for different choices of L and R , using both Brownian Dynamics and Monte Carlo simulations.

The relevant test of the dynamical Monte Carlo (DMC) algorithm reliability is the acceptance ratio Υ , i.e. the number of accepted Monte Carlo moves as compared to the number of attempts, which must be close to 1. Indeed, in Monte Carlo algorithms, a move is always accepted if $\Delta U \leq 0$ and is accepted with probability $\exp(-\Delta U/k_B T)$ if $\Delta U > 0$. Thus $\Upsilon \simeq 1/2 + \langle \exp(-\Delta U/k_B T) \rangle_{\Delta U > 0} / 2 \simeq 1 - \langle \Delta U \rangle_{\Delta U > 0} / (2k_B T)$ and the condition $\Delta U \ll k_B T$ is equivalent to Υ close to 1.

We have observed that, up to error bars, statistical and dynamical properties are similar. In terms of acceptance ratio Υ , we have measured that our Monte Carlo parameter choices lead to $60\% < \Upsilon < 90\%$ for all the situations studied in this paper. Thus the criterion $\Delta U \ll k_B T$ is not satisfied *stricto sensu*, but the fact that both types of simulations give comparable results even at the dynamical level proves that this value of Υ is sufficient in our case. The choice of excluded volume interaction in the DMC code (whenever a move would lead to the penetration of a bead into an other one or the substrate, it is rejected) saves computational time as compared to the calculation of truncated Lennard-Jones potentials used in Brownian Dynamics. Since DMC is favorable in terms of computational time (about 30 times faster in our case because it saves the computation of Lennard-Jones potentials and allows for a larger time step), we restrict our numerical work in the paper to DMC simulations. Note however that these Monte Carlo simulations remain time-consuming: each simulation for a set of parameters typically requires one week on a standard processor.

Exact equilibrium distributions in the rigid and flexible limits

The particle center distribution $G(\mathbf{r}_0, \mathbf{r}; N)$ is the polymer propagator from $\mathbf{r}_0 = \mathbf{0}$ to the center of the particle \mathbf{r} , in N steps (in the $z > 0$ half-space). The experimental observable is not this full distribution but the marginal distribution of ρ

$$p(\rho) = 2\pi\rho \int_{R-a}^{z_{\max}(\rho)} G(\mathbf{0}, \mathbf{r}; N) dz, \quad (\text{S5})$$

where $z_{\max}(\rho) = \sqrt{(R_0 + L)^2 - \rho^2}$ is the maximum value for z at fixed ρ and $R_0 \equiv R + a$ (Fig. S1). This probability distribution can be computed analytically in the two following limits: rigid rod ($L/\ell_p \rightarrow 0$) and phantom Gaussian chain ($L/\ell_p \rightarrow \infty$). In the rigid rod limit,

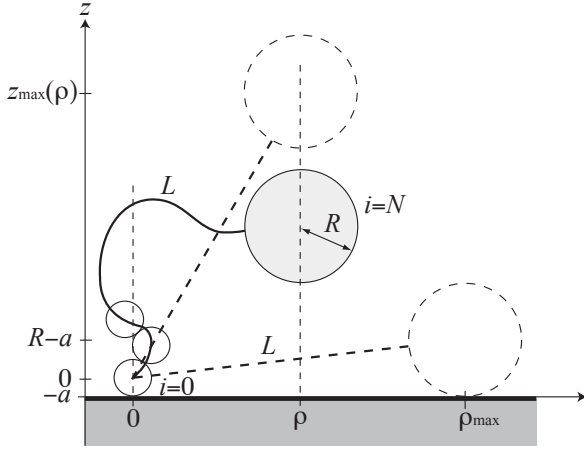


FIG. S1: TPM geometry. The particle has radius R . The polymer, of curvilinear length L , is modeled by a sequence of N spheres of radius a . The polar coordinates of the particle in the (xy) plane are denoted by (ρ, φ) , ρ_{\max} is the maximum extension and the particle height is denoted by z . The whole chain is confined in the upper half-space. For a given ρ , $z \leq z_{\max}(\rho)$. Only ρ and φ (or x and y) are accessible by TPM.

the propagator is simply fixed by $|\mathbf{r}| = R_0 + L$, in other words $G_{RR}(\mathbf{0}, \mathbf{r}; N) = A \delta[\sqrt{\rho^2 + z^2} - (R_0 + L)]$ where $A = [2\pi(R_0 + L)(2a + L)]^{-1}$ is the normalization constant. Using Eq. (S5), we find

$$p_{RR}(\rho) = \frac{\rho}{(2a + L)\sqrt{(R_0 + L)^2 - \rho^2}} \quad (\text{S6})$$

for $0 \leq \rho \leq \rho_{\max} \equiv \sqrt{(R_0 + L)^2 - (R - a)^2}$ (Fig. S1). In Fig. S2a, we display $p_{RR}(u)$ where $u \equiv \rho/\rho_{\max}$. This distribution is linear for small ρ . When $R \ll L$, it sharply increases for $\rho \rightarrow \rho_{\max}$ because of projection effects. When $R \gg L$, this distribution becomes $p_{RR}(u) \simeq 2u$, owing to $p_{RR}(u) = p_{RR}(\rho) d\rho/du = \rho_{\max} p_{RR}(\rho)$.

In the flexible or phantom Gaussian regime, the end-to-end distance probability distribution for the chain alone

is given by $G_{\text{chain}}(\mathbf{0}, \mathbf{r}_{N-1}; N-1) \propto \exp\{-3\mathbf{r}_{N-1}^2/[2(N-1)(2a)^2]\}$, where \mathbf{r}_{N-1} is the 3D position of the last sphere. The distribution of the center of the particle \mathbf{r} is obtained by imposing that $|\mathbf{r} - \mathbf{r}_{N-1}| = R_0$:

$$\begin{aligned} P(\mathbf{r}) &\equiv G_G(\mathbf{r}_0, \mathbf{r}; N) = \int d^3\mathbf{r}_{N-1} G_{\text{chain}}(\mathbf{0}, \mathbf{r}_{N-1}; N-1) \\ &\quad \times \delta(|\mathbf{r} - \mathbf{r}_{N-1}| - R_0) \\ &= B\alpha^{3/2} \frac{\sinh(2\alpha R_0|\mathbf{r}|)}{\alpha R_0|\mathbf{r}|} \exp[-\alpha(\mathbf{r}^2 + R_0^2)], \end{aligned} \quad (\text{S7})$$

a function of $|\mathbf{r}|$ where $\alpha = \frac{3}{2(N-1)(2a)^2}$. The constant B is given by the normalization condition $\int_V P(\mathbf{r}) d^3\mathbf{r} = 1$, V being the accessible volume. In order to forbid polymer trajectories intersecting the $z = 0$ plane, we subtract all the forbidden paths using the mirror reflection argument [1] (the mirror image of $z = 0$ is in the notation of Fig. S1, $z = -2a$):

$$\begin{aligned} p_G(\rho) &= 2\pi\rho \left[\int_{R-a}^{z_{\max}(\rho)} P(\sqrt{\rho^2 + z^2}) dz \right. \\ &\quad \left. - \int_{R-a}^{z_{\max}(\rho)} P(\sqrt{\rho^2 + (z + 2a)^2}) dz \right] \quad (\text{S8}) \\ &= 2\pi\rho \left[\int_{R-a}^{z_{\max}(\rho)} P(\sqrt{\rho^2 + z^2}) dz \right. \\ &\quad \left. - \int_{R+a}^{z_{\max}(\rho) + 2a} P(\sqrt{\rho^2 + z^2}) dz \right], \end{aligned} \quad (\text{S9})$$

as plotted in Fig. S2b. The analytical expression for $p_G(\rho)$ is rather complicated but mean values such as $\langle \rho^2 \rangle \equiv \langle \mathbf{r}_{\parallel}^2 \rangle \equiv \Delta \mathbf{r}_{\parallel}^2$ can, in principle, be computed without major difficulty. This probability distribution can be simplified in two limits. For small particle radii, $R \ll \sqrt{La}$, Eq. (S9) reads

$$\begin{aligned} p_G(\rho) &\approx 2\pi^{3/2} B \alpha \rho e^{-\alpha(\rho^2 + R_0^2)} \times \\ &\quad \{ \text{erf}[\sqrt{\alpha}(R + a)] - \text{erf}[\sqrt{\alpha}(R - a)] \\ &\quad - \text{erf}[\sqrt{\alpha}(z_{\max}(\rho) + 2a)] + \text{erf}[\sqrt{\alpha}z_{\max}(\rho)] \} \\ &\approx 2\alpha \rho e^{-\alpha\rho^2}, \end{aligned} \quad (\text{S10})$$

where $\text{erf}(x) = \frac{2}{\sqrt{\pi}} \int_0^x e^{-y^2} dy$ is the error function. As expected, we recover the Gaussian behaviour when $R \rightarrow 0$ and $\langle \rho \rangle = \sqrt{\pi} \sqrt{aL/3}$ and $\langle \rho^2 \rangle = 4aL/3$, which corresponds to Eq. (10c) of Ref. [2] in the limit $R \ll \sqrt{La}$ (with $\xi = a$).

In the large particle radius limit, $R \gg \sqrt{La}$, we find $P(\mathbf{r}) \simeq \sqrt{\alpha} \exp[-\alpha(|\mathbf{r}| - R)^2]/(R|\mathbf{r}|)$ and the most probable value for $|\mathbf{r}|$ gets displaced towards non-zero values $\langle |\mathbf{r}| \rangle = R$. Equation (S9) then simplifies to

$$p_G(\rho) \approx 2\sqrt{\frac{\alpha}{\pi}} \frac{\rho}{\sqrt{\rho^2 + R^2}} \exp[-\alpha(\rho^2 + 2R^2 - 2R\sqrt{\rho^2 + R^2})]. \quad (\text{S11})$$

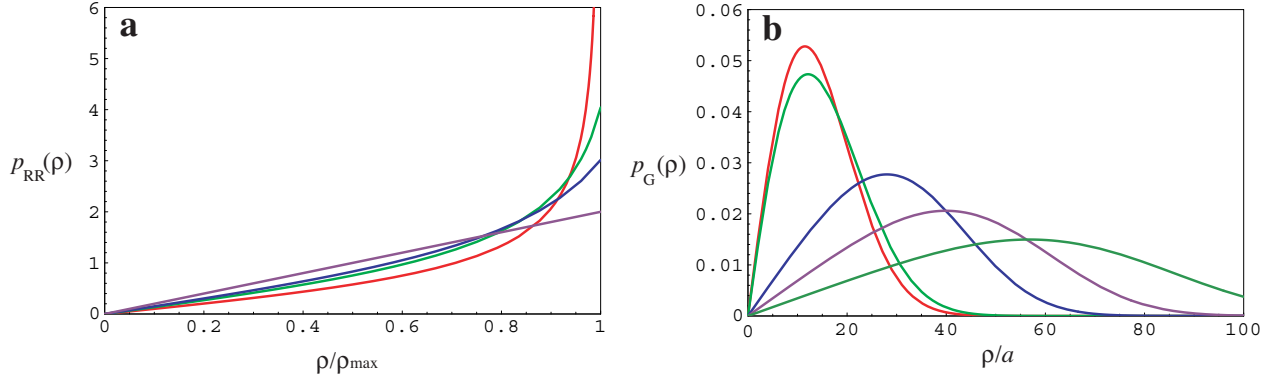


FIG. S2: Theoretical probability distribution $p(\rho)$ for $N = 100$ in the two following limits. (a): Rigid rod for various particle sizes R : a (red), $L/2$ (green), L (blue), and ∞ (purple) (from top to bottom at $u = 1$). $p_{RR}(u)$ is expressed as a function of the reduced particle coordinate parallel to the substrate, $u \equiv \rho/\rho_{\max}$. (b): Gaussian chain, $p_G(\rho)$, ρ in units of a and various particle sizes R : 0 [pure Gaussian see Eq. (S10)], $10a$, $50a$, $100a$, and $200a$ from left to right.

When R increases, this probability distribution gets displaced to the right and widens as seen in Fig. S2b. But due to the projection in 2D, the most probable value of ρ now scales like \sqrt{R} and

$$\langle \rho^2 \rangle = \frac{4}{\sqrt{3\pi}} R \sqrt{aL} + \frac{2}{3} aL, \quad (\text{S12})$$

which corresponds to Eq. (10c) of Ref. [2] in the limit $R \gg \sqrt{La}$.

The intermediate semi-flexible regime, $L/\ell_p = \mathcal{O}(1)$, of interest in TPM experiments, is well described by the worm-like chain model. For instance, in the experiments described in the paper, DNA lengths vary between 400 and 2080 bp, which corresponds to $2 < L/\ell_p < 14$. This model can be tackled analytically [3] but it should be kept in mind that real chains are self-avoiding and that the presence of the particle renders the problem even more intricate. For instance, the effect of the excluded volume of the particle is to widen and shift to large ρ the Gaussian distributions shown in Fig. S2b. It then becomes analytically intractable for finite chains, but it can be tackled numerically by Monte Carlo or Brownian dynamics simulations.

In the limit $L \gg \ell_p$ where $\ell_p = 147$ bp is fixed, as for double stranded DNA, the worm-like chain model tends to the Gaussian limit at a more coarse-grained level where the Gaussian unit, the Kuhn length, is no more $2a$ but $2\ell_p$. Moreover the number of independent monomers N becomes $L/2\ell_p$ and the mean-square end-to-end distance is $\Delta \mathbf{r}^2 = \langle \mathbf{r}^2 \rangle = 2L\ell_p$. Hence the formula given by Eq. (S10) is used where the parameter α becomes $\alpha = 3/(4L\ell_p)$. These Gaussian distributions are compared to the numerical ones for $R = 0$ in Fig. 2a of the paper. When $R > 0$, as in Fig. 2b, the numerical distributions cannot be compared to the present theoretical ones because of the excluded volume effect mentioned just above.

Comparison between experimental and numerical distributions

Figures S3 and S4 show experimental and numerical probability distributions $p(\rho)$, in the semi-flexible regime, for DNA of various lengths (from 401 to 2080 bp) and various particle radii.

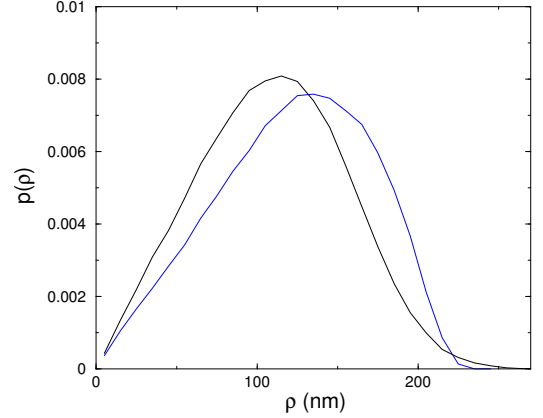


FIG. S3: Experimental (black) and numerical (blue) distributions $p(\rho)$ for $L = 401$ bp and $R = 150$ nm.

Negligible effects of the substrate-DNA joint

Here we address the question of the modeling of the substrate-DNA joint. As already discussed in Ref. [4] in the different context of optically trapped particles, the elastic properties of the polymer's anchor point cannot be well characterized at the experimental level. Therefore we examined two extreme cases: in the paper, we have considered a freely rotating joint (or freely flexible pivot) where all orientations of the chain tangent vec-

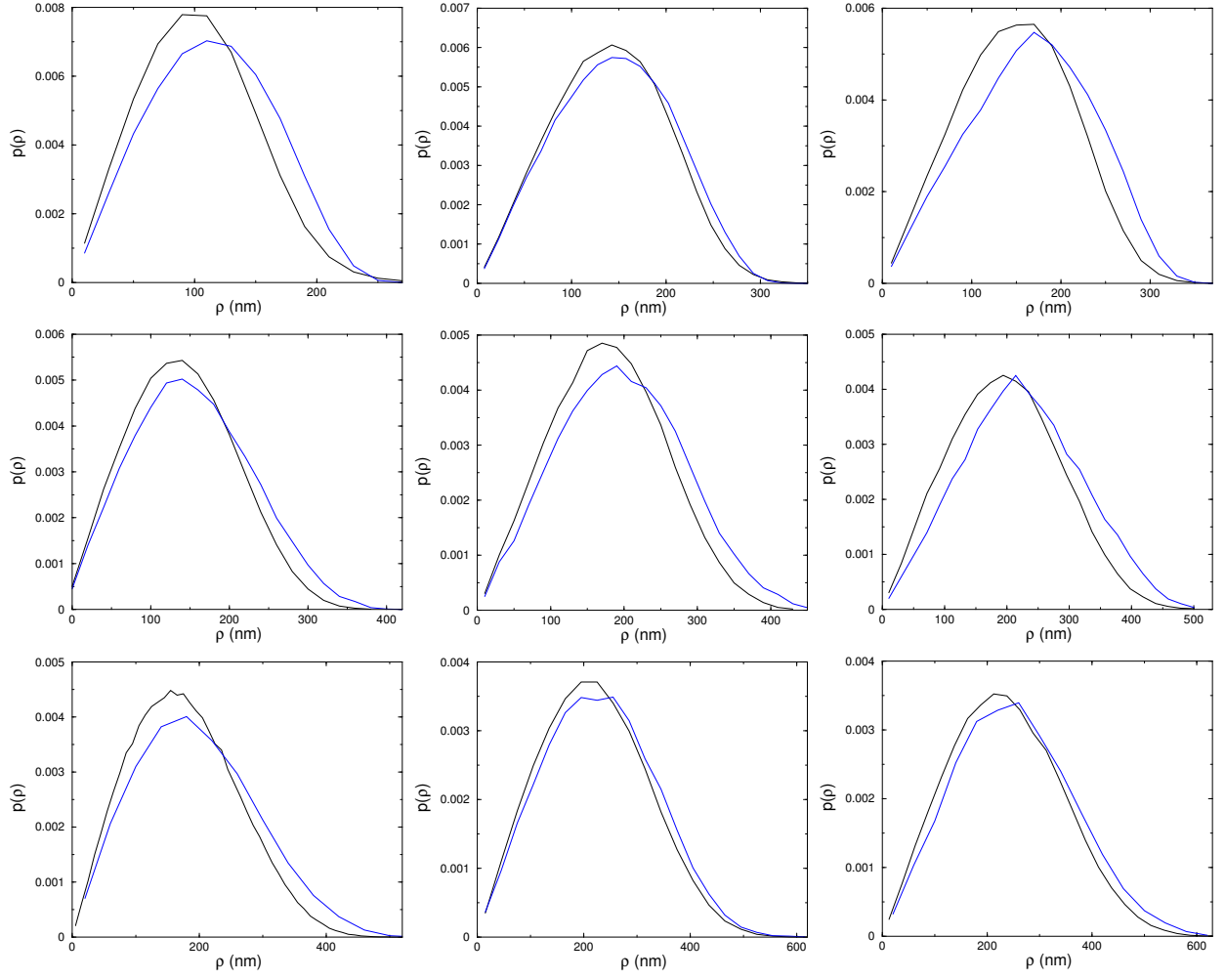


FIG. S4: Experimental (black) and numerical (blue) distributions $p(\rho)$. From top to bottom: $L = 798, 1500, 2080$ bp. From left to right: $R = 20, 100, 150$ nm.

tor close to the substrate are allowed (except, of course, those intersecting the substrate). We also simulated a clamped joint where this tangent vector is prescribed to be perpendicular to the substrate by preventing the second sphere from moving ($\mathbf{r}_1 = 2a\mathbf{e}_z$). *A priori*, only small DNAs are likely to be affected by this boundary condition, because its “memory” along the chain is lost after a few persistence lengths. To clarify this question in the finite L cases considered here, we have also performed DMC simulations with a clamped joint. On the 6 parameter sets studied (namely $L = 401, 798$ and 2080 bp, and $R = 20$ and 150 nm), no clear tendency can be identified: within error bars, τ_{\parallel} (and $\langle \mathbf{r}_{\parallel}^2 \rangle$) are equal in both cases (data not shown). Thus the exact way the joint is modeled is not a relevant issue.

The observed fact that for small particles, the replacement of D_0 by D_{\perp} and D_{\parallel} does not modify τ_{\parallel} , can also be interpreted from this perspective. In this case, the dynamics is dominated by the chain and weakly slowing down the particle does not change this fact. The

only effect of hydrodynamic corrections near the wall is to slow down a few monomer spheres close to the substrate. This can be seen as an intermediate case between the two extreme previous cases: these few spheres are fully mobile when the joint is freely rotating, and immobile when it is clamped. Since these two extreme cases lead to the same relaxation times, the intermediate one – slowed-down spheres – also does.

Measuring the movement amplitude: a comprehensive example

At the end of the Results and Discussion section of the paper, we explain how the relative error on the measure of the movement amplitude $\Delta \mathbf{r}_{\parallel}^2$ decreases with the averaging-interval length, T_{av} :

$$\text{err}(T_{\text{av}}) \equiv \frac{\text{Err}(\mathbf{r}_{\parallel}^2)}{\langle \mathbf{r}_{\parallel}^2 \rangle} \propto \sqrt{\frac{1}{T_{\text{av}}}}. \quad (\text{S13})$$

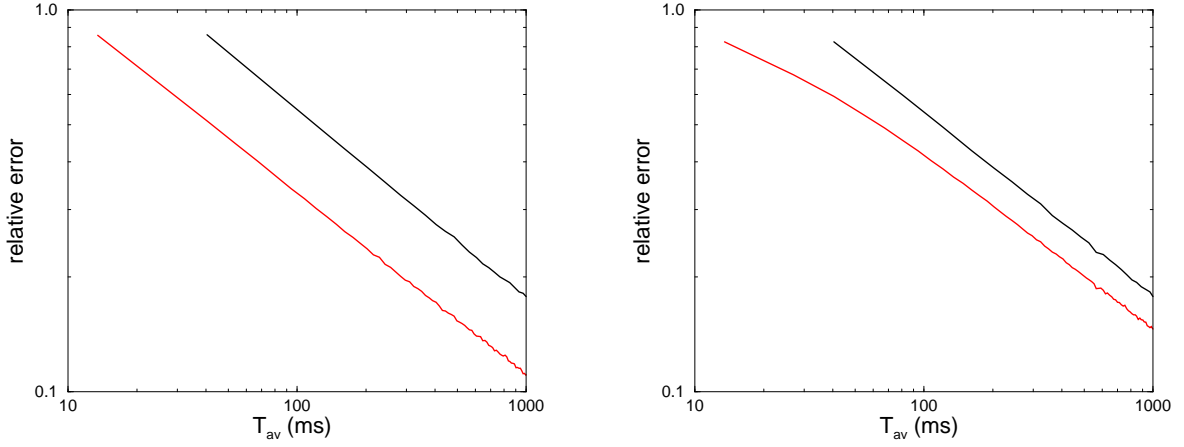


FIG. S5: Relative error $\text{err}(T_{\text{av}})$ on the measure of the amplitude of movement $\langle \mathbf{r}_{\parallel}^2 \rangle$, extracted from experimental data for $L = 2080$ bp and $R = 20$ nm (left) and 100 nm (right). Upper curves: $T_{\text{ac}} = 40.38$ ms; Lower curves: $T_{\text{ac}} = 13.46$ ms. Log-log coordinates.

Figure S5 displays $\text{err}(T_{\text{av}})$ measured for two experimental data sets and two acquisition periods, $T_{\text{ac}} = 13.46$ and 40.38 ms. The second acquisition period is simply mimicked by discarding 2 points over 3 in the data sets. The absolute error $\text{Err}(\mathbf{r}_{\parallel}^2)$ is calculated as the root-mean-square deviation of the measure of $\langle \mathbf{r}_{\parallel}^2 \rangle$ on successive intervals of duration T_{av} . One observes that the slope $-1/2$ at long times is consistent with the expected behavior. At short times, this behavior is potentially affected by the correlation between successive measurements of \mathbf{r}_{\parallel}^2 .

More quantitatively, Eq. (10) of the paper predicts an upper bound for the relative error. In the present case, $\tau_{\parallel} \simeq 8.3$ and 36.3 ms for $R = 20$ and 100 nm, and $\tau_{\parallel,2} \approx$

$\tau_{\parallel}/3$. Thus in the case $R = 100$ nm and $T_{\text{ac}} = 13.46$ ms, $\tau_{\parallel,2} \gtrsim T_{\text{ac}}$ and one expects $\text{err}(T_{\text{av}} = 1\text{s}) < \sqrt{\tau_{\parallel}/T_{\text{av}}} = 0.19$. We obtain experimentally $\text{err}(T_{\text{av}} = 1\text{s}) = 0.15$, in agreement with this upper bound. In the three remaining cases, we are in the regime $\tau_{\parallel,2} \ll T_{\text{ac}}$ and the upper bound becomes $\text{err}(T_{\text{av}} = 1\text{s}) < \sqrt{T_{\text{ac}}/T_{\text{av}}}$ because successive images are uncorrelated. At $T_{\text{ac}} = 40$ ms and $T_{\text{av}} = 1$ s, $\text{err}(T_{\text{av}} = 1\text{s}) < 0.20$, while we measure $\text{err}(T_{\text{av}} = 1\text{s}) = 0.18$ for both radii. Finally, for $R = 20$ nm and $T_{\text{ac}} = 13.46$ ms, the upper bound is 0.12 and we measure 0.11 . In all four cases, the upper bound matches experimental data.

-
- [1] von Smoluchowski, M. 1916. Drei Vorträge über Diffusion, Brownsche Molekularbewegung und Koagulation von Kolloidteilchen. *Phys. Zeit.* 17:557–571.
 - [2] Segall, D. E., P. C. Nelson, and R. Phillips. 2006. Volume-excluded effects in tethered-particle experiments: bead size matters. *Phys. Rev. Lett.* 96:088306.
 - [3] Samuel, J., and S. Sinha. 2002. Elasticity of semiflexible polymers. *Phys. Rev. E* 66:050801(R).
 - [4] Seol, Y., J. Li, P.C. Nelson, T. T. Perkins, and M. D. Betterton. 2007. Elasticity of short DNA molecules: theory and experiment for contour lengths of $0.67 \mu\text{m}$. *Biophys. J.* 93: 4360–4373.